RMetS

Royal Meteorological Society

Influence of microphysical processes on the potential vorticity development in a warm conveyor belt: a case-study with the limited-area model COSMO

H. Joos* and H. Wernli

Institute for Atmospheric and Climate Science, ETH Zurich, Switzerland

*Correspondence to: H. Joos, ETH Zurich, Universitätstrasse 16, CH-8092 Zurich, Switzerland.
E-mail: hanna.joos@env.ethz.ch

The potential vorticity (PV) in warm conveyor belts (WCBs) is strongly influenced by the latent heating associated with the various microphysical processes occurring during the formation of clouds. The first-order effect is that PV increases below the level of maximum diabatic heating and decreases above. Thus, the WCB reaches the upper troposphere with low PV values and has the potential to influence the large-scale dynamics. In order to quantify the influence of different microphysical processes on the diabatic heating rates (DHRs) and associated PV development during the ascent, a Lagrangian analysis is used and applied to a regional model simulation of a selected WCB event. First, the individual DHRs caused by the various microphysical processes are calculated with the COSMO model. Then, the DHRs and the associated changes in PV are evaluated along the WCB trajectories. The relative role of the different microphysical processes is quantified for the latent heating and the diabatic PV modification, for which the gradient of the latent heating and the absolute vorticity are crucially important. It is shown that condensation of vapour and depositional growth of snow each contribute ∼10 K to the total latent heating. However, the diabatic PV modification due to condensation is stronger since it occurs close to the cold frontal low-level maximum of the z-component of the absolute vorticity, η_z, whereas a similar heating rate gradient caused by depositional growth of snow modifies the PV much less since it occurs in a region with much weaker η_z. This highlights the importance of η_z for determining the PV modification due to a certain diabatic heating rate. Furthermore, cooling processes like the evaporation of rain, also co-occurring with high η_z near the surface cold front, have the potential to strongly modify the PV below the WCB. Copyright © 2011 Royal Meteorological Society

Citation: Joos H, Wernli H. 2012. Influence of microphysical processes on the potential vorticity development in a warm conveyor belt: a case-study with the limited-area model COSMO. *Q. J. R. Meteorol. Soc.* **138**: 407−418. DOI:10.1002/qj.934

1. Introduction

Warm conveyor belts (WCBs) are well-defined air streams in extratropical cyclones. They originate in the boundary layer of the warm sector and ascend ahead of the surface cold front (Green *et al.*, 1966; Harrold, 1973; Carlson, 1980). This slantwise ascent represents a dominant feature in extratropical cyclones and is associated with the formation of an elongated cloud band (Browning, 1986). As WCBs rise from the boundary layer to the uppermost troposphere, they

are of great importance for transporting water vapour, heat and trace substances as they connect the different tropospheric sub-layers (Stohl, 2001). Due to the strong vertical motions and the associated formation of clouds, WCBs are responsible for most of the precipitation (Browning, 1986; Wernli, 1997) and meridional energy transport in terms of latent heat in extratropical cyclones (Eckhardt *et al.*, 2004). Furthermore, they influence the formation of ice supersaturated regions and cirrus clouds in the WCB's outflow region due to the transport of ice nuclei and moisture to the upper troposphere (Eckhardt *et al.*, 2004; Spichtinger *et al.*, 2005).

From a climatological standpoint, WCBs are frequent features of midlatitude cyclones, especially during winter. In the Northern Hemispheric winter, a major proportion of cyclones is associated with WCBs ($\sim 60\%$) (Eckhardt *et al.*, 2004). In the Northern Hemisphere, there are two preferential WCB starting regions, east of North America and east of Asia, whereas the WCBs outflow regions in the upper troposphere are located further east, close to the European and North American west coasts (Eckhardt *et al.*, 2004).

WCBs have the potential to influence the upper-tropospheric potential vorticity (PV) pattern as well as to produce low-level positive PV anomalies. This behaviour is based on the fact that latent heat release (occurring in WCBs) can modify the PV. The first-order effect is that PV is produced below the maximum diabatic heating and is destroyed above (Wernli and Davies, 1997). The effect of diabatically produced/destroyed PV on different aspects of cyclone evolution has been investigated in different studies. In general, extratropical cyclones develop due to baroclinic instability but their evolution and intensity can be strongly modified by diabatic processes (e.g. Davis *et al.*, 1993; Rossa *et al.*, 2000). Davis and Emanuel (1991) stated that the formation of a low-level positive PV anomaly produced by condensation might have contributed about 40% of the cyclonic circulation in a mature storm. Stoelinga (1996) showed that the release of latent heat and the associated low-level PV maximum in an extratropical cyclone was responsible for about 70% of the intensity of the surface cyclone. Furthermore they showed that the negative PV anomaly developing above the maximum heating strongly modified the upper-level PV pattern and the evolution of the downstream flow. Posselt and Martin (2004) showed that the existence of an occluded thermal structure was strongly dependent on diabatic heating. These results, among others, show the potential of diabatic heating processes to influence the dynamics in complex ways.

The strong latent heating within WCBs is associated with positive low-level PV tendencies below the maximum diabatic heating and negative PV tendencies in the WCB outflow region. Thus, the typical evolution of PV in a WCB is characterised by low PV values in the lower troposphere (~ 0.5 pvu), followed by an increase to often more than 1 pvu and a subsequent decrease of PV to ~ 0.5 pvu or less (Wernli, 1997). The outflow of a WCB can therefore produce or enhance strong upper-level ridges and consequently modify the downstream evolution of the large-scale flow pattern (Pomroy and Thorpe, 2000). This has also been shown by Massacand *et al.* (2001) who investigated the influence of upstream diabatic heating on the downstream development of a PV streamer that caused a heavy precipitation event to the south of the Alps. They emphasised the importance of accurately modelling the diabatic heating to be able to predict correctly the downstream evolution of the flow. In a similar way, Grams *et al.* (2011) highlight the importance of diabatic heating processes occurring in a WCB for the modification of the midlatitude flow during the extratropical transition of hurricane *Hanna* (2008) and the subsequent development of a Mediterranean cyclone. Dirren *et al.* (2003) found that large forecast errors occur in the region of pronounced upper-level ridges, which might be influenced by WCB outflows. Thus, the correct simulation of diabatic heating and its influence on PV is crucial for the correct simulation of weather systems and the evolution of the downstream flow.

One possibility to identify WCBs is the detection of coherent Lagrangian flow structures (Wernli and Davies, 1997). In order to select trajectories that represent WCBs, they defined a large starting region close to the surface in the atmospheric boundary layer including the warm sector of a developing cyclone. From each gridpoint of the starting region, 48 h forward trajectories were calculated. After that, a criterion was applied to the collection of trajectories that ensures that only WCB trajectories remained in the ensemble. As WCBs are associated with strong latent heating and strong ascent, different criteria, such as a certain decrease in humidity, an increase in potential temperature or a certain ascent (pressure decrease), could be applied in order to identify WCB trajectories. The application of these criteria to the same flow situation to some extent selects the same trajectories (Wernli and Davies, 1997). Here we use a criterion that requires an ascent of more than 600 hPa in 48 h.

In the study presented here, the focus is on determining the contribution of different microphysical processes to the modification of PV in a WCB. Until now, only the influence of the total diabatic heating on the structure of different weather phenomena and the downstream flow evolution has been investigated. However, no studies are available that quantify the contribution of the various microphysical processes occurring in a mixed-phase cloud to the total diabatic heating and to the diabatic modification of PV. As has been shown in several publications (e.g. Szeto and Stewart, 1997; Clough *et al.*, 2000; Forbes and Clark, 2003), ice microphysical processes (e.g. sublimation of ice) can strongly modify the mesoscale structure of cyclones and are therefore of great importance for the correct prediction of surface winds and precipitation. On an even larger scale, if diabatic heating/cooling occuring in WCBs and the associated PV modification is not simulated correctly, forecast errors downstream may occur (e.g. Dirren *et al.*, 2003). It is therefore of great interest to investigate in detail the microphysical processes occuring in a WCB, including the ice phase, that have the potential to modify the PV and to quantify their contribution to the total diabatic PV modification. As WCBs are frequent features in the Northern Hemisphere and have the potential to strongly modify the upper-level PV pattern, our study focuses on the influence of microphysical processes on the PV development in a WCB.

The paper is organised as follows. In section 2 the applied method is explained in detail. In section 3 the microphysical processes important for this study are explained. This is followed by the description of the synoptic situation in section 4, an analysis of the microphysical processes occurring in the COSMO simulation and the associated PV modification in section 5 and a summary of the presented work in section 6.

2. Method

In order to investigate the influence of different microphysical processes on the PV development, simulations with the regional numerical weather prediction model COSMO (COnsortium for Small-scale MOdelling) (Steppeler *et al.*, 2003) are performed. The model is run with a horizontal resolution of 0.25° ($\sim$ 28 km) and 40 vertical levels. ECMWF analysis data are used as initial and boundary data. The WCB ascending from the surface to a height of $\sim$8 km is covered by 29 vertical levels with a decreasing vertical spacing from $\sim$70 m close to the surface to $\sim$600 m at 7 km height. The model contains detailed microphysics with prognostic equations for water vapour q^v, cloud water q^c, cloud ice q^i, rain q^r and snow q^s. (i.e. the superscripts v, c, r, i, and s stand for vapour, cloud water, rain, ice, and snow, respectively). Due to the phase transitions between the different hydrometeor species, latent heat is released leading to various diabatic heating/cooling rates (DHRs). These DHRs are calculated within the model and written out every timestep (15 min for the present study). The total DHR is therefore given by the sum over all DHRs caused by the 14 different microphysical processes:

$$(DHR)_{\text{tot}} = \sum_{p=0}^{13}(DHR)_p, \qquad (1)$$

where p is the index of the considered process, namely condensation/evaporation of cloud water, evaporation of rain, heterogeneous nucleation of cloud ice, homogeneous nucleation of cloud ice, depositional growth/sublimation of cloud ice, melting of cloud ice, autoconversion of cloud ice to form snow due to deposition, collection of cloud water by snow (riming), collection of cloud ice by rain to form snow, freezing of rain due to collection of cloud ice to form snow, freezing of rain due to heterogeneous nucleation to form snow, depositional growth/sublimation of snow, melting of snow and convection. In this case-study, since convection occurs mainly behind the cold front and is therefore not seen by the WCB trajectories, the DHR caused by convection is not discussed in the following analysis. The most important processes are explained in more detail in section 3.

According to Hoskins *et al.* (1985), PV can be modified by diabatic processes as follows:

$$DPVR = \frac{\text{D}}{\text{D}t}PV = \frac{1}{\rho}\boldsymbol{\eta}\cdot\nabla(DHR) \approx \frac{1}{\rho}\eta_z\cdot\frac{\partial}{\partial z}(DHR), \quad (2)$$

where D/Dt denotes the material derivative and $\boldsymbol{\eta}$ the absolute vorticity vector. The modification of PV due to frictional processes is neglected here. The main effect of the diabatic heating is therefore a production of PV below the maximum of the DHR and a depletion of PV above under the assumption that the vertical gradient of the DHR is larger than the horizontal gradient. With Eq. (2), a corresponding diabatic PV rate (DPVR) is calculated for each component of the DHR described above such that the influence of the different microphysical processes on the PV development can be investigated separately. The total DPVR is then given by the sum over all DPVRs,

$$(DPVR)_{\text{tot}} = \sum_{p=0}^{13}(DPVR)_p, \qquad (3)$$

with p denoting the same microphysical processes as in Eq. (1). Thus, the DPVRs are calculated at all gridpoints in the whole model domain from the instantaneous DHRs that are written out every 15 min. An additional simulation where the DHRs have been accumulated over the previous hour shows only slight differences to the instantaneous values of the DHR and the calculated DPVRs. This implies that the latent heat release is more or less constant within time intervals of 1 h.

Using the COSMO simulation output and the calculated DHRs and DPVRs, forward trajectories are run with the trajectory tool LAGRANTO (Wernli and Davies, 1997) and the DHR and DPVR as well as the pressure p, potential temperature θ, PV and the vertical component of $\boldsymbol{\eta}$ are tracked along the trajectories. The timestep used for the trajectory calculations is 75 s and the output is written every 15 min like the output frequency of the COSMO simulation. In order to investigate WCBs, a starting region in the warm sector of the cyclone associated with the WCB is defined. Thereafter, 48 h forward trajectories are calculated from every gridpoint in the starting region. In order to identify WCB trajectories, the selection criterion of an ascent larger than 600 hPa within 48 h was applied. This criterion has been shown to be reasonable for selecting WCB trajectories if the ascent occurs in the vicinity of a low pressure system (Wernli and Davies, 1997; Eckhardt *et al.*, 2004).

3. Microphysical processes

In this section, the most important processes influencing the PV in our case-study are explained in more detail. Doms *et al.* (2007) give a complete description of the COSMO microphysics. The microphysics scheme used in this study is operational in the global model of the German Weather Service (DWD) which runs at a resolution of 30 km. It is therefore tested thoroughly and can be used at a resolution of 28 km.

Temperature changes by phase transitions between the different water categories can be described by

$$\frac{\partial T}{\partial t} = \frac{L_{\text{V}}}{c_{pd}}(S^c + S^r) + \frac{L_{\text{S}}}{c_{pd}}(S^i + S^s), \qquad (4)$$

where L_{V} and L_{S} are, respectively, the latent heat of vapourisation and of sublimation, and the terms S^x describe the source and sink terms for the indicated water category due to various microphysical transfers between the different hydrometeor species. The source and sink terms are given by

$$S^c = S_c - S^c_{\text{frz}} + S^i_{\text{melt}} - S_{\text{rim}} + S_{\text{nlh}}, \qquad (5)$$

$$S^i = S_{\text{nuc}} + S^c_{\text{frz}} + S^i_{\text{dep}} - S^i_{\text{melt}} - S_{\text{aud}} - S^i_{\text{cri}} + S_{\text{nlh}}, \qquad (6)$$

$$S^r = S_{\text{ev}} + S_{\text{shed}} - S^r_{\text{cri}} - S^r_{\text{frz}} + S^s_{\text{melt}} + S_{\text{nlh}}, \qquad (7)$$

$$S^s = S_{\text{aud}} + S_{\text{rim}} + S^s_{\text{dep}} + S^i_{\text{cri}} + S^r_{\text{cri}} + S^r_{\text{frz}} - S^s_{\text{melt}} + S_{\text{nlh}}, \qquad (8)$$

where the terms S_x denote the individual microphysical processes represented in the model (Table I).

The terms S_{nlh} summarise additional processes like autoconversion or accretion where no latent heat is released. These processes are not included in the following discussion.

As will be shown below, the main contribution to the DHR in the present case are from condensation/evaporation, depositional growth/sublimation and melting of snow, and

Table I. Abbreviation and description of the microphysical processes considered.

Abbreviation	Description
S_{aud}	Autoconversion of cloud ice to form snow due to deposition
S_c	Condensation and evaporation of cloud water
S_{ev}	Evaporation of rain
S_{nuc}	Heterogeneous nucleation of cloud ice
S_{rim}	Collection of cloud water by snow (riming)
S_{frz}^{c}	Nucleation of cloud ice due to homogeneous freezing of cloud water
S_{cri}^{i}	Collection of cloud ice by rain to form snow
S_{dep}^{i}	Depositional growth and sublimation of cloud ice
S_{melt}^{i}	Melting of cloud ice to form cloud water
S_{cri}^{r}	Freezing of rain due to collection of cloud ice to form snow
S_{frz}^{r}	Freezing of rain due to heterogeneous nucleation to form snow
S_{dep}^{s}	Depositional growth and sublimation of snow
S_{melt}^{s}	Melting of snow to form rain water

the evaporation of rain. The parametrisations of these processes in the COSMO model are therefore explained in more detail. For the other processes and additional information on the processes explained here, the reader is referred to Doms *et al.* (2007).

The treatment of the condensation/evaporation process is based on saturation adjustment. If a gridbox becomes supersaturated with respect to water during a time step, the excess water vapour is instantaneously transferred to cloud water. If it becomes subsaturated the cloud water is evaporated until saturation is reached or no cloud water is left. In this method no activation of cloud condensation nuclei (CCN) is calculated and it is assumed that there are always enough CCNs present for cloud droplets to form (Doms *et al.*, 2007).

The depositional growth/sublimation of snow is parametrised according to the mass growth equation (e.g. Prupacher and Klett, 1997) which, integrated over the size distribution of snow, is given by

$$S_{dep}^{s} = c_{dep}^{s} \left\{ 1 + b_{dep}^{s} (\rho q^s)^{5/24} \right\} \left(q^v - q_{si}^v \right)^{2/3}, \quad (9)$$

where ρ denotes the density of air, q_{si}^v saturation specific humidity with respect to ice, $c_{dep}^{s} = 3.2 \times 10^{-2}$ and $b_{dep}^{s} = 14.7$. As the saturation specific humidity of ice is smaller than for water ($q_{si}^v < q_{sw}^v$), large supersaturations with respect to ice can occur in cold clouds. Therefore, if the air is supersaturated with respect to ice (i.e. $q^v > q_{si}^v$), snow crystals grow due to vapour deposition inside clouds whereas they sublimate if the air becomes subsaturated (i.e. $q^v < q_{si}^v$). Furthermore, the same supersaturation leads to more vapour deposition if more q^s is available.

The evaporation of rain is parametrised similarly:

$$S_{ev} = \alpha_{ev} \left\{ 1 + \beta_{ev} (\rho q^r)^{3/16} \right\} \left(q_{sw}^v - q^v \right)^{1/2}, \quad (10)$$

where q_{sw}^v denotes the saturation specific humidity with respect to water, $\alpha_{ev} = 3.1 \times 10^{-3}$ and $\beta_{ev} = 9.0$. In contrast to the depositional growth of snow, the diffusional growth of raindrops vanishes within clouds as the saturation adjustment scheme removes the supersaturation with respect to water. Thus, raindrops can only evaporate below cloud where the air becomes subsaturated with respect to water (i.e. $q^v < q_{sw}^v$) whereas the rate of change increases with increasing rain mass q^r. The constants $c_{dep}^{s}, b_{dep}^{s}, \alpha_{ev}$ and β_{ev} include a dependence on the terminal fall velocities of snow crystals and rain droplets, respectively.

For the parametrisation of melting of snow, it is assumed that the release of latent heat from melting is balanced by the heat flux between the particle and the ambient air. Integrating over the size distribution of snow crystals yields

$$S_{melt}^{s} = c_{melt}^{s} \left\{ 1 + b_{melt}^{s} (\rho q^s)^{5/24} \right\} \\ \times \left[(T - T_0) + a_{melt}^{s} \{ q^v - q_{sw}^v (T_0) \} \right] (\rho q^s)^{2/3}, \quad (11)$$

where $T_0 = 273.15$ K denotes the freezing temperature and T the ambient temperature, $c_{melt}^{s} = 1.48 \times 10^{-4}$, $b_{melt}^{s} = 14.37$ and $a_{melt}^{s} = 2.31 \times 10^3$. Thus, in addition to the dependence of the melting rate on the ambient temperature, it depends also on the specific humidity. If the air surrounding the melting snow is subsaturated with respect to water the melting rate of snow can be decreased by evaporation of water vapour from the melted snow. Due to the saturation adjustment, this process can only occur below cloud base. In section 5, the DHRs caused by these processes as well as the corresponding DPVRs will be discussed.

4. Synoptic overview and general characteristics of the WCB

4.1. WCB in ECMWF analyses

For our study on the microphysical processes in a WCB, a WCB associated with a cyclone that developed in the eastern North Atlantic has been selected.

Figure 1 shows the ECMWF analyses from 0600 UTC on 29 January 2009 to 0600 UTC on 31 January 2009, which corresponds to the time period where the cyclone intensified and the WCB was strongest. Initially, the cyclone was located near 20°W, 50°N below the downstream flank of a positive upper-level PV anomaly in a strong baroclinic zone (Figure 1(a, b)). One day later, the cyclone strongly intensified and reached a minimum surface pressure of ~ 975 hPa. Furthermore, distinct surface cold and warm fronts and a pronounced warm sector reaching from Spain to southern Scandinavia can be seen in the 850 hPa potential temperature field (Figure 1(d)). At this time, the upper-level PV pattern shows a strong elongated ridge with low PV values aligned with the warm sector (Figure 1(c)). In the following 24 h, the cyclone travels further to the north while decaying. The PV on the 310 K isentrope reveals an intense and large negative PV anomaly extending from ~ 45°N to 80°N over western Europe (Figure 1(e)). In its northernmost
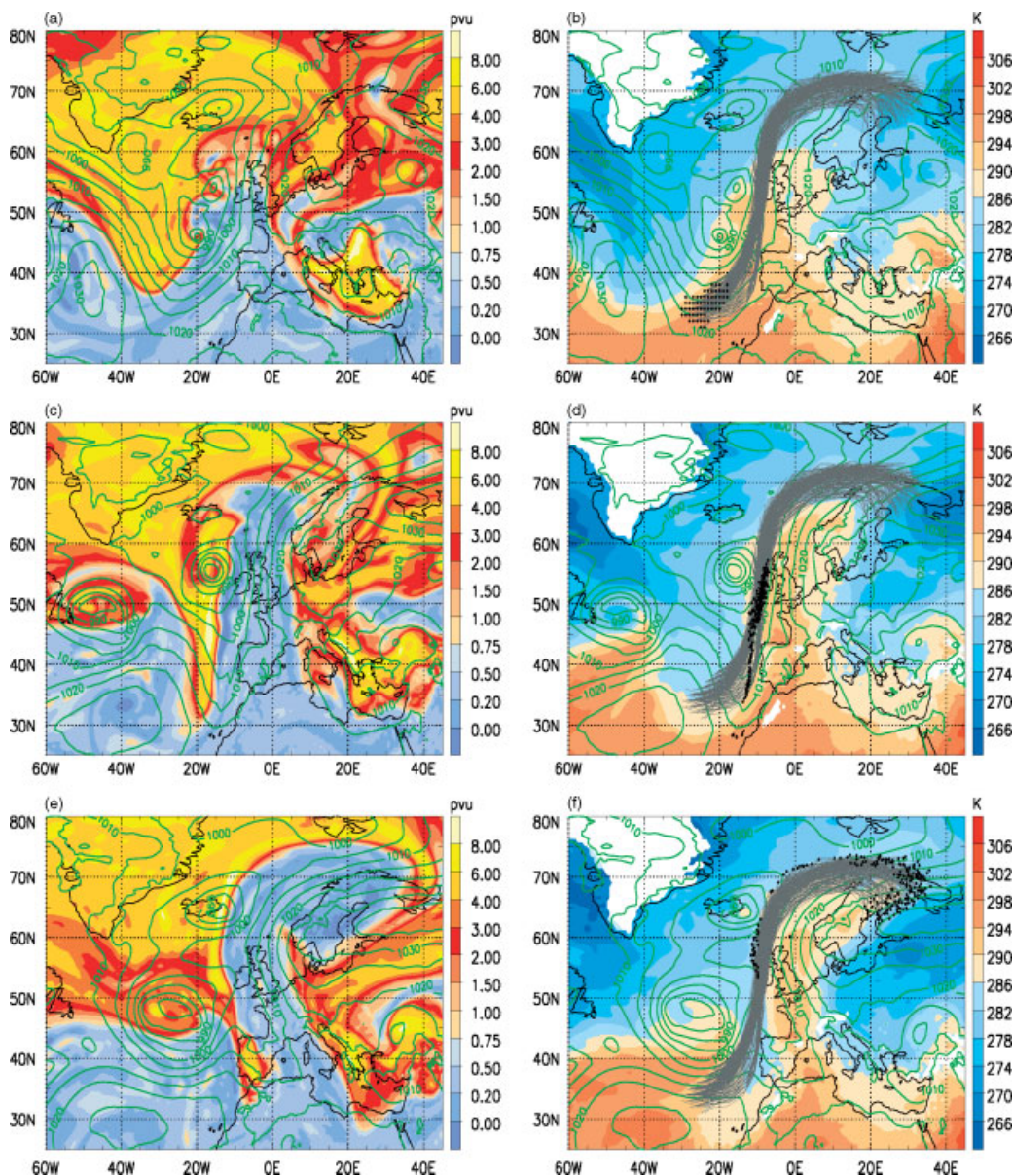
Figure 1. (a, c, e) Time evolution of PV on the 310 K isentrope (pvu, colour shading) and sea level pressure (SLP, green contours with interval 5 hPa). (b, d, f) Potential temperature at 850 hPa (K, colour shading), SLP (green contours with interval 5 hPa) and 48 h WCB – trajectories started at 0600 UTC on 29 January 2009 (grey lines): 0600 UTC 29 January (a,b), 0600 UTC 30 January (c,d), 0600 UTC 31 January (e,f). Black dots denote the position of the air parcels along the trajectories at the same point in time as the SLP field. All data are taken from the ECMWF operational analyses.

part it is deflected to the east and is present over the entire Scandinavian region.

A strong WCB is associated with this cyclone. Its starting region at 0600 UTC on 29 January is located around 35°N in the atmospheric boundary layer (below 800 hPa) $\sim$ 1700 km to the south of the cyclone centre (Figure 1(b)). The first air parcels start to ascend around 0000 UTC on 29 January, however most of the air parcels exhibiting a 600 hPa ascent in 48 h start 6 h later at 0600 UTC on 29 January. In the following 24 h, the air parcels start ascending while moving towards the north in the warm sector and pass the cyclone centre to the east (Figure 1(d)). At the end of their ascent the air parcels reach a height of about 300 hPa while travelling poleward to 70°N where they are deflected eastwards. The WCB outflow is located downstream of the associated cyclone (Figure 1(f)). Thus the WCB corresponds to a strong poleward transport event of moisture and heat. During the ascent, clouds form, the specific humidity decreases strongly

and latent heat is released. The air parcels are heated by about 20 K leading to a strong cross-isentropic flow. Due to the latent heat release, the PV is strongly modified during the ascent. Initial PV values are 0.5 pvu in the mean, and they reach a maximum of 0.8 pvu near 900 hPa before returning to fairly low PV values of 0.1 pvu in the outflow. This temporal evolution of PV and potential temperature is consistent with earlier WCB case-studies (e.g. Wernli and Davies, 1997; Grams *et al.*, 2011). As long as the trajectories are located below the maximum DHR, PV is produced whereas it is destroyed above. The WCB therefore leads to the formation of a positive low-level PV anomaly and strongly modifies the upper-level PV pattern as it brings air with low PV values to the upper troposphere. In the case presented here, the WCB contributes to the building of a large region with negative PV anomalies around the 310 K isentrope which expands along the whole European coast (Figure 1(c, d)).
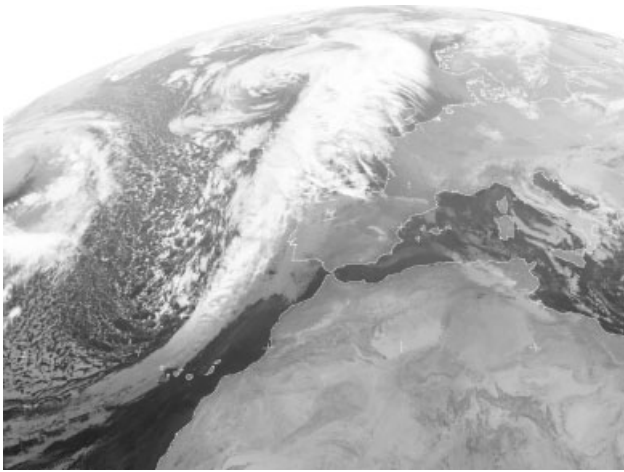
Figure 2. Meteosat SEVIRI infrared satellite image valid for 0600 UTC on 30 January 2009 (from http://www.neodaas.ac.uk/).

The existence of the WCB is quantitatively confirmed by satellite imagery. Figure 2 shows the Meteosat SEVIRI infrared satellite image valid at 0600 UTC on 30 January, i.e. at the time when the WCB air parcels are located in a narrow band extending from the west of Portugal to Ireland (Figure 1(d)).

An elongated cloud band along the European west coast can be seen, collocated with the rising WCB. The satellite picture shows nicely the cloud-forming mechanism of the WCB.

4.2.   WCB in COSMO simulation

In Figure 3 the results for the upper-level PV pattern, the potential temperature at 850 hPa and the WCB trajectories from the COSMO simulation are shown. First of all, a good agreement of the large-scale synoptic features with the ECMWF analyses can be seen. Figure 3(a) corresponds to the point in time where the trajectories reach the upper troposphere after their 48 h ascent (0600 UTC on 31 January). The pronounced ridge at the 310 K isentrope is simulated well, although slight differences to the ECMWF data can be seen over southern Scandinavia. The SLP is also simulated realistically for both points in time shown here. The green dots show the intersection points of the WCB outflow with the 310 K isentrope. The WCB trajectories are situated in the negative PV anomaly, highlighting again the WCB modification of the upper-level PV pattern. Figure 3(b) shows the potential temperature at 850 hPa and SLP 24 h after the start of the WCB trajectories (e.g. at 0600 UTC on 30 January) and the WCB trajectories calculated with LAGRANTO based on the COSMO output (note that only every fiftieth trajectory is plotted). The applied selection criteria of an ascent of at least 600 hPa in 48 h selects 10288 trajectories. Compared to Figure 1(c, d), the potential temperature distribution as well as the WCB trajectories agree well, although the bunch of trajectories is less coherent in the COSMO simulation than in the ECMWF analyses, especially in the outflow region. However, the comparison of the synoptic conditions simulated by COSMO with the ECMWF data reveals an adequate representation of the considered low pressure system and associated WCB so that the COSMO simulation can be used to investigate the effect of microphysical processes on the WCB in section 5.

4.3.   Lagrangian characteristics of the WCB

Figure 4 shows the evolution of the potential temperature θ, PV, the vertical component of the absolute vorticity η_z, and the total DHR along the ascending WCB trajectories.

As the trajectories are strongly heated during the ascent, θ increases by $\sim$20 K from 290 K to 310 K and the trajectories reach the upper troposphere. The evolution of the PV along the WCB trajectories matches the typical behaviour with low PV values around 0.5 pvu close to the surface, increasing PV values in the lower troposphere below the maximum diabatic heating with values of up to 1.5 pvu, and again decreasing values above such that the WCB reaches the upper troposphere with low PV values below 0.5 pvu, and therefore contributes to the formation of a pronounced upper-level ridge (Figure 3(a)). The low-level PV maximum is situated around 900 hPa, relatively close to the surface. The vertical component of the absolute vorticity η_z shows high values between $2 \times 10^{-4} \text{s}^{-1}$ and $4 \times 10^{-4} \text{s}^{-1}$ as long as the air parcels are located close to the surface cold front where the WCB starts its ascent; lower values of about 0 to $1 \times 10^{-4} \text{s}^{-1}$ with increasing height appear when the WCB trajectories are located above the cold front or in the outflow region. During their ascent, the trajectories are heated with values up to 2 K h^{-1} over a large pressure range reaching from 900 hPa to a height of $\sim$ 500 hPa.

In Figure 5 the most important components of the DHR occurring in the WCB are integrated along each trajectory during the 48 h ascent in order to show the contribution of each process to the total latent heating.

In total, the trajectories are heated between 15 K and 25 K. The largest contribution with $\sim$10 K arises from the condensational heating in the lower part of the cloud. However, the depositional growth of snow contributes to the total latent heating with nearly the same amount ($\sim$10 K). Further positive contributions come from convection and the depositional growth of cloud ice (not shown). Additionally, the trajectories are cooled mainly due to the evaporation of rain but also due to the melting of snow. For WCB trajectories, the heating strongly dominates. This leads to an increased ascent and to the strong cross-isentropic flow observed in WCBs. This picture provides a clear indication of the important contribution of ice phase processes to the diabatic heating in WCBs.

5.   Analysis of microphysical processes

5.1.   Vertical sections across the WCB

In order to investigate in detail the influence of the different microphysical processes on the PV, vertical cross-sections through the WCB are discussed. In Figures 6, 7, 8, 9 a vertical cross-section is shown through the WCB from 20 to 10°W at 38°N at 0000 UTC on 30 January, i.e. 18 h after the start of the WCB trajectories.

5.1.1.   Hydrometeor distribution

In Figure 6, the mass of the different hydrometeor species is depicted. The cloud associated with the WCB extends from the surface up to 400 hPa. In the lower parts of the troposphere at temperatures above 0°C, the cloud consists of cloud water and rain. At temperatures below 0 °C, a mixed-phase cloud with a coexisting liquid and ice phase
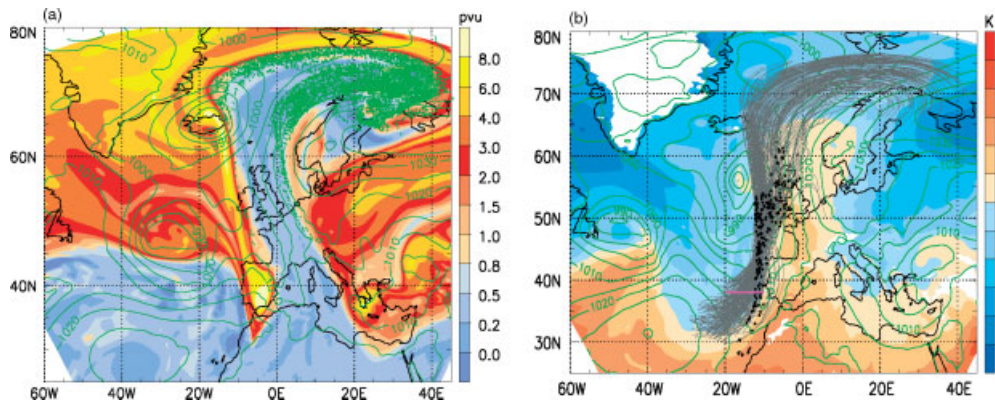
Figure 3. (a) Trajectory intersection points (green dots) with the 310 K isentrope at 0600 UTC on 31 January 2009, with PV on 310 K surface (pvu, colour shading) and SLP (green contours with interval 5 hPa). (b) Potential temperature at 850 hPa (K, colour shading), SLP (green contours with interval 5 hPa) at 0600 UTC on 30 January, 24 h after the start of the WCB trajectories and 48 h WCB – trajectories started at 0600 UTC on 29 January (grey lines). Black dots denote the position of the air parcels along the trajectories at the same point in time as the SLP field and the pink line shows the position of the vertical cross-section shown in Figures 6, 7, 8, 9. Note that only every fiftieth trajectory is plotted.
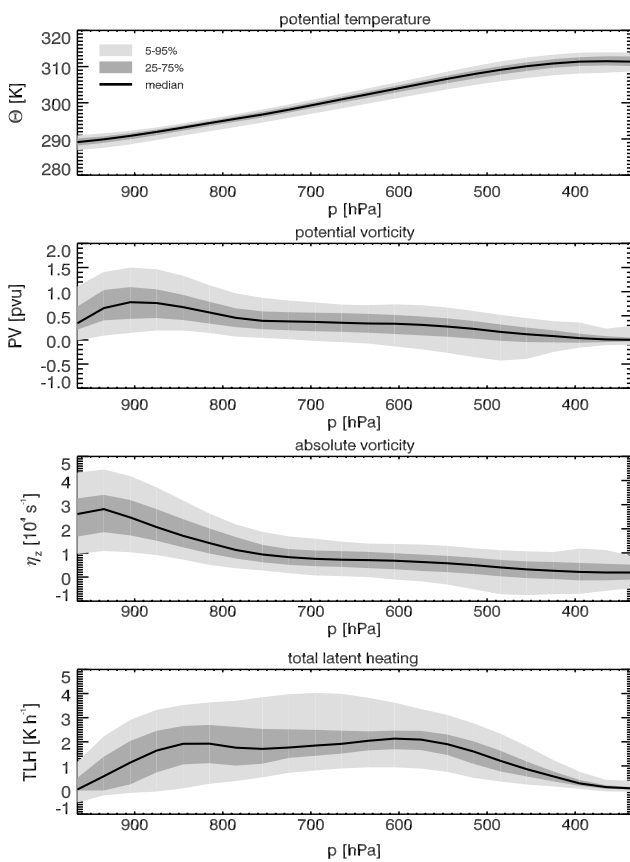

Figure 4. Evolution along trajectories of potential temperature θ, PV, z-component of the absolute vorticity η_z, and total latent heating. Grey shaded areas denote the 5–95% and 25–75% percentiles, and black lines show the median over all trajectories.

exists whereas in the upper part, the cloud is completely glaciated consisting of snow and ice. The lines for different temperatures show where different freezing mechanism can be active in the COSMO model. Heterogeneous freezing occurs only where the temperature is below $-6\,°C$ and the air is saturated with respect to water. Thus, in the temperature range between 0 and $-6\,°C$, only falling snow particles and no cloud ice are present. At temperatures below $-25\,°C$, cloud ice can form due to deposition freezing (direct transfer from water vapour to ice) if the air is supersaturated
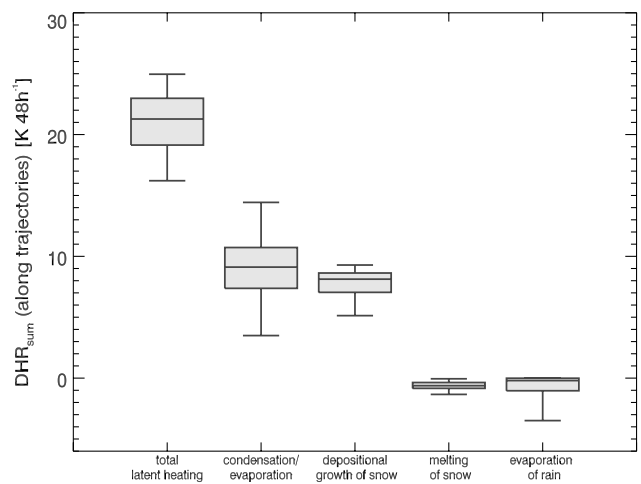

Figure 5. Integrated DHR along trajectories for the total latent heating and the most significant contributing processes: condensation/evaporation, depositional growth of snow, melting of snow and evaporation of rain. The box shows the 25–75% range and the bars the 5–95% percentiles.
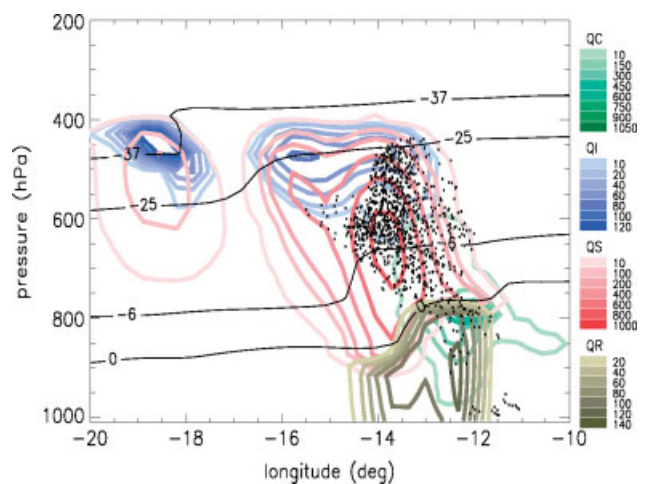

Figure 6. Vertical cross-section at 0000 UTC on 30 January through the WCB at 38°N. Coloured lines denote the mass of the different hydrometeor species in mg kg^{-1}: green lines cloud water, blue lines cloud ice, red lines snow, and brown lines rain. The black lines show different temperatures important for the parametrisation of freezing in COSMO (0 °C, $-6\,°C$, $-25\,°C$ and $-37\,°C$ isotherms) and the black dots denote the intersection points of the WCB trajectories with the cross-section at this time ±15 min. The position of the cross-section is shown as the pink line in Figure 3(b).
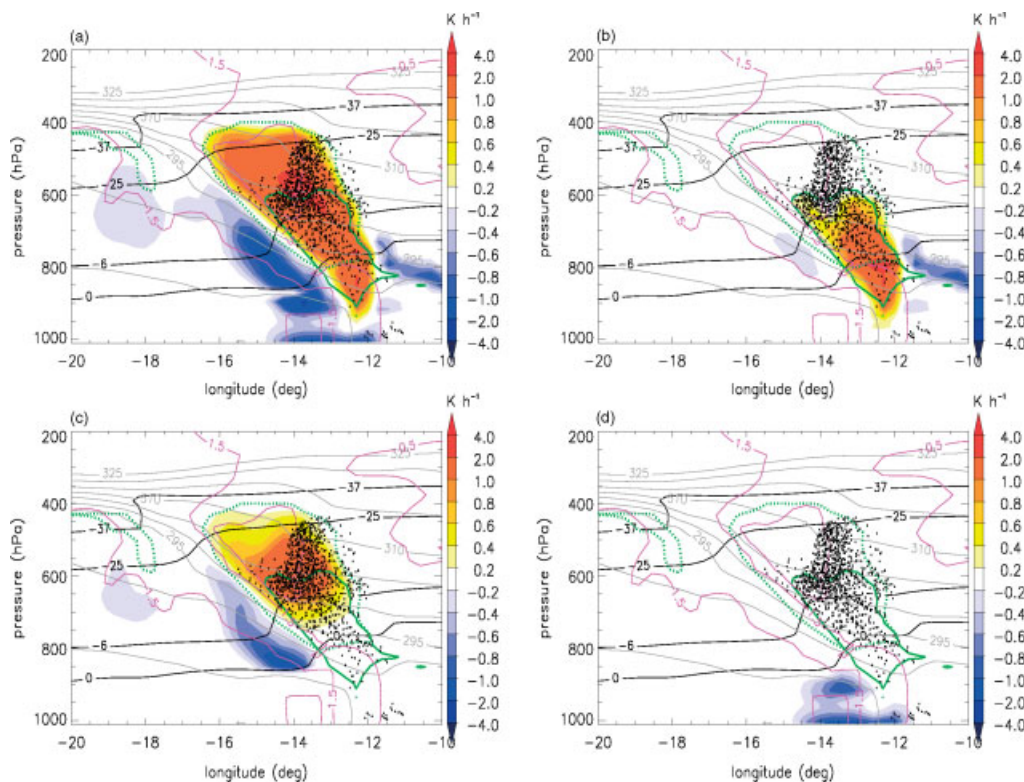
Figure 7. Vertical cross-section at 0000 UTC on 30 January through the WCB at 38°N. Colour shading denotes (a) the total DHR, (b) the DHR caused by condensation/evaporation, (c) by the depositional growth of snow, and (d) by the evaporation of rain (all K h^{-1}). Grey lines show the potential temperature, black solid lines different temperatures important for the parametrisation of freezing in COSMO (0°C, −6°C, −25°C and −37°C), green lines denote 99% relative humidity with respect to water (solid) and with respect to ice (dotted) and pink lines show the z-component of the absolute vorticity η_z (values of 0.5 and 1.5×10^{-4}s^{-1}). The position of the cross-section is shown as the pink line in Figure 3(b).

with respect to ice. Homogeneous freezing of cloud droplets begins at temperatures below −37 °C, however this process does not occur in the WCB. The black dots show the intersection points of the WCB trajectories with this cross-section at the time shown here ±15 min. The trajectories are located in the middle of the cloud, in a region where snow is the dominant hydrometeor category.

5.1.2. Diabatic heating rates

Figure 7 shows the most important DHRs in the same vertical cross-section through the WCB. The formation of clouds in the WCB leads to a strong latent heat release of up to 4 K h^{-1} near 600 hPa. Below the WCB a region of strong latent cooling with values of −2 K h^{-1} can be seen in the total latent heating rate (Figure 7(a)). Most of the WCB trajectories are located in the heated branch. The strong latent heating leads to the strong cross-isentropic flow of the trajectories observed in WCBs. In the lower part of the cloud at temperatures above 0 °C, the formation of cloud water leads to latent heat release due to condensation (Figure 7(b)). This process contributes most to the total latent heating in the warm part of the cloud. However, it can be seen that condensation is also active in a region with temperatures below 0 °C. As the heterogeneous freezing of cloud droplets starts only if the temperature drops below −6 °C and the air is saturated with respect to water, condensation is important for all temperatures above −6 °C. At temperatures below −6 °C only few ice crystals form. This process and the subsequent depositional growth of ice (or snow) is not efficient enough to remove enough water vapour such that the relative humidity with respect to water drops below

100%. Thus, the saturation adjustment can still be active even below −6 °C. The fact that no ice can be seen at temperatures slightly below −6 °C can be attributed to the fast depositional growth of ice crystals to the size of snow such that, in the vertical section shown here, ice can be seen only around −25 °C where depositional freezing is active.

In the mid-troposphere, the depositional growth of snow, i.e. the transfer of water vapour directly to snow crystals, exhibits a major part of the total latent heating (Figure 7(c)). Furthermore, a strong cooling region can be seen below the heated region. The cooling is produced by falling snow crystals that start to sublimate below cloud base as the air is subsaturated with respect to ice in this region (green dashed line). The same effect can be seen for the evaporation of rain droplets close to the surface where the air is subsaturated with respect to water (Figure 7(d), green solid line). On the one hand, the conveyor belt therefore produces regions of strong heating due to the cloud formation but, on the other hand, strong cooling regions can form below the WCB due to the sublimation or evaporation of falling hydrometeors. The importance of cooling processes like evaporation, sublimation or melting for the mesoscale dynamics and frontogenesis has been highlighted in various studies (e.g. Huang and Emanuel, 1991; Parker and Thorpe, 1995; Szeto and Stewart, 1997; Clough *et al.*, 2000; Forbes and Clark, 2003; Forbes and Hogan, 2006) but will not be considered in detail here.

The cross-section shown here has been selected in order to illustrate the microphysical processes occurring in the WCB in the middle of its ascent. In sections across the WCB more to the south (i.e. at earlier times), the trajectories are located closer to the surface where condensation is
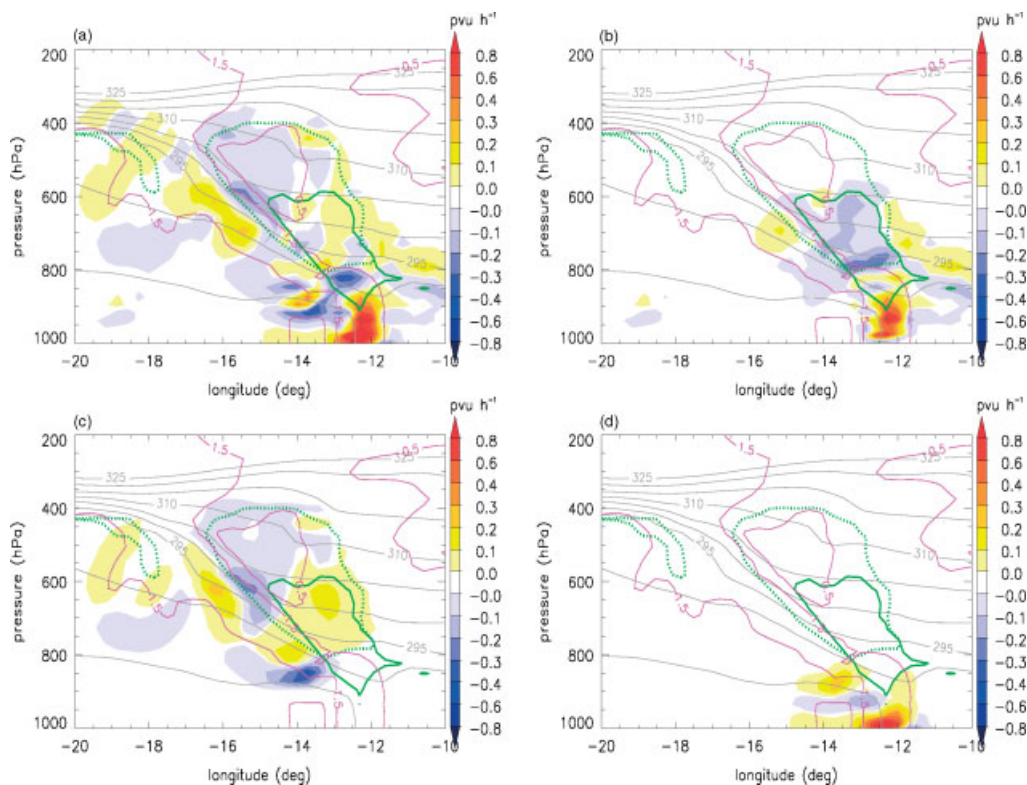
Figure 8. Vertical cross-section at 0000 UTC on 30 January through the WCB at 38°N. Colour shading denotes the DPVR (pvu h^{-1}) caused by (a) the total latent heating, (b) the condensation/evaporation, (c) the depositional growth of snow and (d) evaporation of rain. Other details are as in Figure 7.
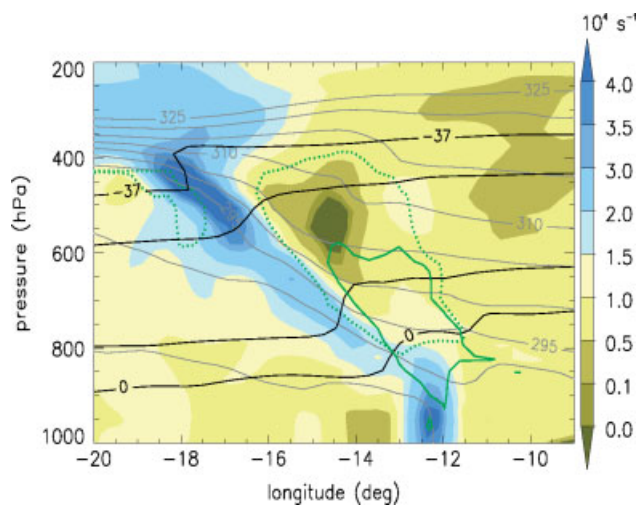

Figure 9. Vertical cross-section at 0000 UTC on 30 January through the WCB at 38°N, with colour shading denoting the vertical component of the absolute vorticity η_z. Other details are as in Figure 7.

the main contribution to the total latent heating. In WCB cross-sections further north, the ice phase is dominant as only high clouds exist and the trajectories are located in the upper troposphere where they are mainly influenced by depositional growth of snow and ice.

5.1.3. Diabatic PV modification

The vertical cross-sections of the DPVRs associated with these DHRs are shown in Figure 8.

The DPVR is calculated according to Eq. (2). It depends on the gradient of the DHR as well as on the absolute vorticity. In the case shown here, the vertical gradient of the DHR is larger than the horizontal gradients. Thus, in order to understand the pattern of the DPVR, a cross-section of the z-component of the absolute vorticity η_z is also shown in Figure 9. The DPVR associated with the total latent heating (Figure 8(a)) reveals a fairly noisy pattern. As the vertical gradient of the DHR dominates, a positive (negative) DPVR below (above) the maximum DHR could be expected. However, as the DPVR additionally depends on the absolute vorticity, such a simple pattern would occur only if absolute vorticity were more or less constant in the region where the DHR occurs. Since η_z varies strongly in the vicinity of the front, this behaviour cannot be seen in the total DPVR. However, if considering the DPVR associated with individual microphysical processes, relatively simple patterns occur (e.g. Figures 8(b, d)). Condensation/evaporation and the evaporation of rain occur in regions with fairly constant values of η_z, leading to dipolar patterns of DPVR associated with these DHR maxima. In general, whether a vertical gradient in the DHR has a small or a large influence on the DPVR depends on η_z at the location of the gradient. In the case presented here, the strongest η_z occurs along the cold front (Figure 9) coinciding with a region of strong DHR associated with condensation of cloud water and evaporation of rain. Therefore, the DPVR caused by these processes is strong and clearly evident in the total DPVR (Figure 8(a)). In contrast, the strong DHR due to depositional growth of snow coincides with a region of small η_z values, for which reason the influence of this microphysical process on the PV is much weaker (Figure 8(c)). It has to be mentioned here that the DPVR is calculated as described in Eq. (2), thus taking into account all contributions to the scalar product between absolute vorticity and the gradient of DHR. The DPVR fields shown
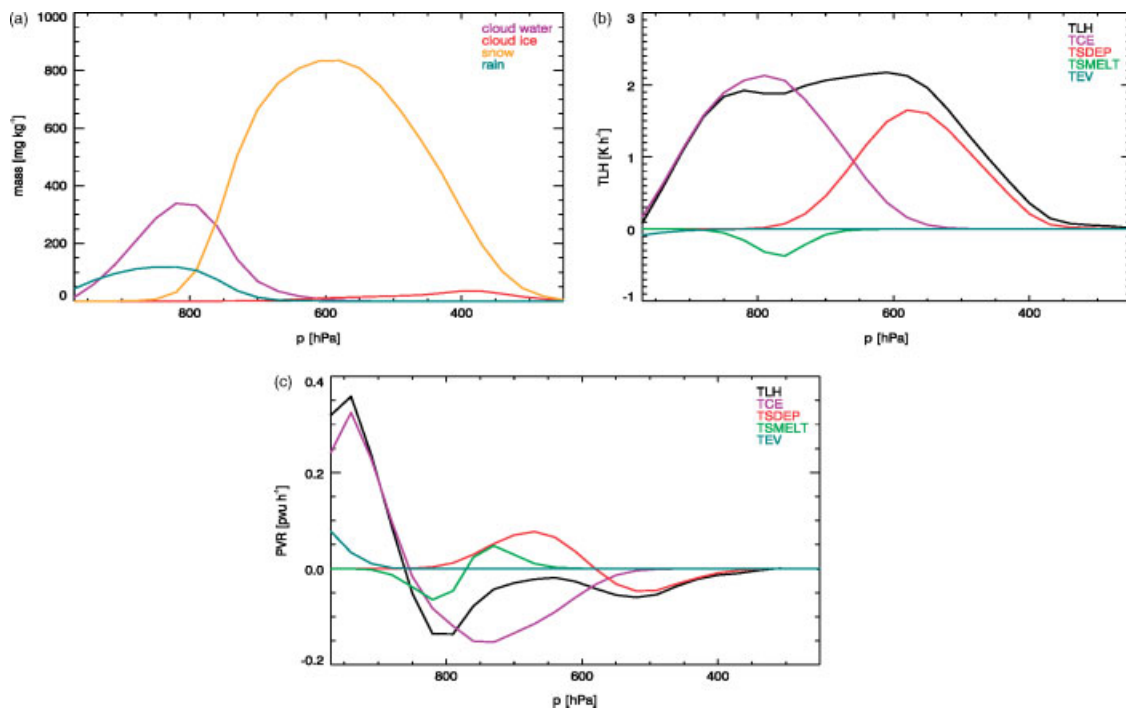
Figure 10. Evolution of the mean over all WCB trajectories of (a) hydrometeor mass, (b) DHR and (c) DPVR. In (b, c), the black lines show the DHR and the corresponding total DPVR (TLH), and coloured lines show the contributions from the different microphysical processes to the total DHR (DPVR): condensation/evaporation (TCE), depositional growth of snow (TSDEP), melting of snow (TSMELT), and evaporation of rain (TEV).

in the vertical cross-sections therefore contain also the contributions from the horizontal derivatives of the DHRs and the x- and y-components of the absolute vorticity. Our qualitative consideration of only the z-component can explain the observed features in first order but small effects from the other components show up as well.

5.2. Evolution along trajectories

In order to investigate the influence of the various microphysical processes on the PV evolution of the WCB, the individual DHR and corresponding DPVR fields are tracked along the trajectories. From the total latent heating (Figure 4), the change in PV along the WCB trajectories cannot be inferred directly. However, if the total latent heating is separated into the contributions from the different microphysical processes and the evolution of η_z along the trajectories is taken into account, a meaningful analysis of the PV modification due to the different processes is possible. Figure 10 shows the evolution of the different hydrometeor species, the DHR and corresponding DPVR for the processes contributing most to the total DHR as a mean over all trajectories.

As long as the trajectories are located in a region with temperatures above 0 °C, condensation occurs and cloud water forms (Figure 10(a), purple line). Additionally, falling rain (or melted snow) is seen by the trajectories (turquoise line). When the air parcels rise, more vapour is condensed leading to an increase of cloud water and rain with height. With further ascent, the temperature decreases and the trajectories reach a region where snow is formed (yellow line), and later, at lower temperatures, the trajectories cross an area where cloud ice occurs (red line). Note that the formation of the different hydrometeor species does not necessarily take place at the moment when the ascending trajectories cross this area. It is therefore not possible to

estimate the latent heat release due to a certain formation process from the total mass of the considered hydrometeor species. The hydrometeors that are seen by the trajectories are to some extent already present during the passage and are only partly formed while the trajectories pass the considered region.

The latent heat release associated with the formation of the hydrometeors is shown in Figure 10(b) for the processes that contribute most to the total DHR. The trajectories are heated from the low levels until a height of ~400 hPa (Figure 10(b), black line). Two different maxima appear in the total DHR that can be attributed to different microphysical processes. The first maxima is produced by condensation at lower levels leading to the formation of cloud water. This process is the main source of latent heating at these levels and reaches values of up to 2 K h^{-1} (purple line). With the increase in height and the formation of snow, condensation becomes less important and the depositional growth of snow is the main sink for water vapour. The contribution from the depositional growth is only slightly smaller than that from condensation (red line). Furthermore, the temporal gradients of these two DHRs are very similar and symmetric around their particular maximum. Additionally, two cooling processes are shown. The falling rain starts to evaporate and cool the environment close to the surface (turquoise line). The amount of cooling is relatively weak, however, and it is confined to a narrow layer close to the surface. Another important cooling process is the melting of snow when it falls into regions above 0 °C (green line).

Figure 10(c) shows the evolution of the DPVR associated with the different microphysical processes described above. The total DPVR (black line) shows strong PV production below 850 hPa. Above, the DPVR becomes negative leading to diabatic PV destruction, which is less pronounced but lasts upto a height of 400 hPa. If only the total DHR is considered, the shape of the PV evolution and total DPVR cannot be

understood easily. However, if the total DPVR is split into the contributions from the different microphysical processes and the evolution of η_z is considered as well, the behaviour of the total DPVR can be explained. The first peak of the total DPVR is produced by condensation (purple line). Below the maximum DHR due to condensation (Figure 10(b), purple line) the DPVR is positive and PV is produced, whereas it becomes negative when the trajectories are located above the maximum DHR due to condensation (Figure 10(c), purple line). The evolution of the total DPVR in the lower levels is mainly determined by this process. Although the DHR due to condensation exhibits a fairly symmetric shape and therefore gradients of the same magnitude with opposite signs below and above the maximum (also Figure 7(b)), the corresponding DPVR does not show a symmetric behaviour. The DPVR is much larger at low levels where η_z is particularly large (Figure 4). The evaporation of rain, leading to a cooling, amplifies the positive DPVR at low levels (turquoise line) as the air parcels gain PV if they are situated above a cooling region. This process also occurs in a region with very high η_z values, leading to a strong influence of this process on the PV. At a height of ~ 800 hPa, the depositional growth of snow starts to release a large amount of latent heat and therefore leads to the production of PV below its maximum at 550 hPa and a destruction above (red line). Again, the shape of the associated DPVR is not symmetric as η_z strongly varies along the trajectories with higher values below the maximum DHR. Thus the PV production due to depositional growth of snow is more pronounced than the PV destruction, although the gradient of the DHR above and below the maximum is nearly equal (also Figure 7(c)). Between 800 and 600 hPa, the DPVR due to depositional growth of snow counteracts the modification of PV due to condensation. As the gradient of the DPVR due to depositional growth of snow at a height of 750 hPa is much smaller than the corresponding gradient in the DHR due to condensation at this height, and η_z does not differ much for both processes, the production of PV due to depositional growth of snow can only partly offset the PV destruction due to condensation. The melting of snow amplifies the PV destruction below 750 hPa, but also increases the PV production due to depositional growth of snow above this level. In summary, the breakdown of the total DHR and DPVR into the different contributions allows for an understanding of the evolution of the total DPVR, and eventually PV, along the WCB.

A second case-study of a WCB in January 2005 starting at the US East Coast has been investigated in order to estimate how representative these results are. The results are very similar to the ones presented here. Condensation accounts for $\sim 60\%$ of the total diabatic heating along trajectories, whereas depositional growth of snow contributes with 40%. The modification of PV caused by the different microphysical processes also reveals a very similar behaviour. At low levels, PV is produced mainly by condensation whereas it is produced by depositional growth of snow at levels higher than 800 hPa. Also the asymmetric shape of the curves caused by decreasing absolute vorticity values along the trajectories can be seen in this case. These results give us some confidence that the observed features may be generalized to some degree also for other WCBs, although some details are definitely different for each case.

6. Summary

In this article, the influence of microphysical processes on the PV development in a WCB has been investigated. A case-study of a WCB occurring on 29–31 January 2009 has been simulated with the regional NWP model COSMO. During this period, a low pressure system developed in the eastern North Atlantic associated with a strong WCB reaching from 30 to 70°N. The WCB outflow occurred at a height of ~ 300 hPa on the 310 K isentrope. The WCB reached the upper troposphere with low PV values below 0.5 pvu contributing to the formation of a pronounced upper-level ridge. The question of which microphysical processes contribute to the PV modification during the ascent has been investigated in detail by looking at the contributions from different microphysical processes separately.

Therefore, the DHRs arising due to the different microphysical processes as represented in the COSMO model have been analysed based upon very frequent model output. Based on these DHRs, the associated DPVR have been calculated for each process and evaluated along objectively identified WCB trajectories. In addition, the potential temperature, PV, and the vertical component of the absolute vorticity η_z have been tracked along the trajectories.

The ascending air in the WCB leads to the formation of clouds consisting of cloud liquid water, rain, cloud ice, and snow. During the formation of the different hydrometeor species, latent heat is released. In the case-study discussed here, the ascending air parcels experience a heating of ~ 10 K due to condensation and 10 K due to depositional growth of snow, respectively, which represent the most important heating processes in this WCB. Furthermore, the trajectories undergo a weak cooling due to melting of snow and evaporation of rain. Thus, the WCB produces a region of strong heating due to the formation of clouds but also strong cooling regions develop mainly below the WCB due to the evaporation/sublimation or melting of the sedimenting hydrometeor species rain and snow (Figure 7).

The strength of the modification of PV due to a certain DHR depends on the gradient of the DHR as well as on the absolute vorticity occurring in the considered region. In the case considered here, a band of high values of η_z occurs along the sloping cold frontal surface (Figure 9). The DHRs occurring in this region, i.e. condensation and evaporation of rain, therefore exhibit a strong DPVR. Although the DHRs due to depositional growth and the associated gradient are on the same order of magnitude, this process occurs in a region with smaller values of η_z and the influence on PV is much less pronounced (Figures 8, 9). The vertical component of the absolute vorticity η_z therefore plays a key role in determining the effect of different microphysical processes on the PV modification.

The evolution of the DHR along the WCB trajectories shows two distinct maxima. The first maximum is produced by condensation whereas the second maximum occurs due to the depositional growth of snow. The amount of heating due to these processes as well as the DHR gradients are similar (Figure 10(b)). However, the corresponding DPVRs differ from each other. Again, as the condensation occurs in a region with high values of η_z, the associated DPVR is larger than for depositional growth in particular at low levels where the DPVR is positive. Hence, the PV destruction above

850 hPa due to negative vertical gradients of the DHR due to condensation is not fully compensated by the positive DPVR due to depositional growth of snow at slightly higher levels. This again highlights the importance of the evolution of η_z along the WCB trajectories for the diabatic modification of PV. The separation of the contributions from the different DHRs allows for understanding of the evolution of PV along the WCB and highlights the complex potential of various microphysical processes to modify the PV in this important airstream.

It has to be mentioned here that the results depend on the parametrisation of microphysical processes in COSMO. However, as the model is able to capture the observed flow features quite well, it can also be assumed that the simulated DHRs and DPVRs associated with the cloud formation might represent realistic features. We emphasise that other parametrisations (in other models) would yield some differences in the detailed structure of the DHRs and DPVRs without affecting the overall picture. Clearly, it will be important to test the robustness of the presented results, e.g. in a model intercomparison project.

This study demonstrates the complex interaction between small-scale microphysical processes occurring in a WCB and the large-scale flow. It has been shown that many different microphysical processes, in particular condensation, evaporation of rain and depositional growth/sublimation of snow can modify the PV in a complex way. This result on the importance of microphysical processes for the mesoscale structure of PV in extratropical cyclones is in line with earlier studies (e.g. Parker and Thorpe, 1995; Szeto and Stewart, 1997; Clough *et al.*, 2000; Forbes and Hogan, 2006). With regard to the improvement of weather prediction models, it could be useful to investigate in more detail the representation of diabatic processes and their manifold influence on the large- and mesoscale dynamics, in WCBs and other flow features associated with extratropical weather systems.

Acknowledgements

References

Browning KA. 1986. Conceptual models of precipitation systems. *Weather Forecasting* **1**: 23–41.

Carlson TN. 1980. Airflow through midlatitude cyclones and the comma cloud pattern. *Mon. Weather Rev* **108**: 1498–1509.

Clough SA, Lean HW, Roberts NM, Forbes RM. 2000. Dynamical effects of ice sublimation in a frontal wave. *Q. J. R. Meteorol. Soc.* **126**: 2405–2434.

Davis CA, Emanuel KA. 1991. Potential vorticity diagnostic of cyclogenesis. *Mon. Weather Rev.* **119**: 1929–1953.

Davis CA, Stoelinga MT, Kuo Y-H. 1993. The integrated effect of condensation in numerical simulations of extratropical cyclogenesis. *Mon. Weather Rev.* **121**: 2309–2330.

Dirren S, Didone M, Davies HC. 2003. Diagnosis of 'forecast–analysis' differences of a weather prediction system. *Geophys. Res. Lett.* **30**: 20, DOI: 10.1029/2003GL017986

Doms G, Förstner J, Heise E, Herzog H-J, Raschendorfer M, Reinhardt T, Ritter B, Schrodin R, Schulz J-P, Vogel G. 2007. '*A description of the non-hydrostatic regional model LM, Part II: Physical parameterization*'. Deutscher Wetterdienst: Offenbach, Germany.

Eckhardt S, Stohl A, Wernli H, James P, Forster C, Spichtinger N. 2004. A 15-year climatology of warm conveyor belts. *J. Climate* **17**: 218–237.

Forbes RM, Clark PA. 2003. Sensitivity of extratropical cyclone mesoscale structure to the parametrization of ice microphysical processes. *Q. J. R. Meteorol. Soc.* **129**: 1123–1148.

Forbes RM, Hogan RJ. 2006. Observations of the depth of ice particle evaporation beneath frontal cloud to improve NWP modelling. *Q. J. R. Meteorol. Soc.* **132**: 865–883.

Grams CM, Wernli H, Boettcher M, Campa J, Corsmeier U, Jones SC, Keller JH, Lenz C-J, Wiegand L. 2011. The key role of diabatic processes in modifying the upper-tropospheric wave guide: a North Atlantic case-study. *Q. J. R. Meteorol. Soc.* **137**: 2174–2193.

Green JSA, Ludlam FH, McIlveen JFR. 1966. Isentropic relative-flow analysis and the parcel theory. *Q. J. R. Meteorol. Soc.* **92**: 210–219.

Harrold TW. 1973. Mechanisms influencing the distribution of precipitation within baroclinic disturbances. *Q. J. R. Meteorol. Soc.* **99**: 232–251.

Hoskins BJ, McIntyre ME, Robertson AW. 1985. On the use and significance of isentropic potential vorticity maps. *Q. J. R. Meteorol. Soc.* **111**: 877–946.

Huang H, Emanuel KA. 1991. The effects of evaporation on frontal circulations. *J. Atmos. Sci.* **48**: 619–628.

Massacand AC, Wernli H, Davies HC. 2001. Influence of upstream diabatic heating upon an Alpine event of heavy precipitation. *Mon. Weather Rev.* **129**: 2822–2828.

Parker DJ, Thorpe AJ. 1995. The role of snow sublimation in frontogenesis. *Q. J. R. Meteorol. Soc.* **121**: 763–782.

Pomroy HR, Thorpe AJ. 2000. The evolution and dynamical role of reduced upper-tropospheric potential vorticity in Intensive Observing Period 1 of FASTEX. *Mon. Weather Rev.* **128**: 1817–1834.

Posselt DJ, Martin JE. 2004. The effect of latent heat release on the evolution of a warm occluded thermal structure. *Mon. Weather Rev.* **132**: 578–599.

Pruppacher HR, Klett JD. 1997. *Microphysics of clouds and precipitation*. Kluwer Academic:

Rossa AM, Wernli H, Davies HC. 2000. Growth and decay of an extra-tropical cyclone's PV-tower. *Meteorol. Atmos. Phys.* **73**: 139–156.

Spichtinger P, Gierens K, Wernli H. 2005. A case study on the formation and evolution of ice supersaturation in the vicinity of a warm conveyor belt's outflow region. *Atmos. Chem. Phys.* **5**: 973–987.

Steppeler J, Doms G, Schättler U, Bitzer HW, Gassmann A, Damrath U, Gregoric G. 2003. Meso-gamma scale forecast using the nonhydrostatic model LM. *Meteorol. Atmos. Phys.* **82**: 75–96. DOI: 10.1007/s00703-001-0592-9

Stoelinga MT. 1996. A potential vorticity-based study of the role of diabatic heating and friction in a numerically simulated baroclinic cyclone. *Mon. Weather Rev.* **124**: 849–874.

Stohl A. 2001. A 1-year Lagrangian 'climatology' of airstreams in the Northern Hemisphere troposphere and lowermost stratosphere. *J. Geophys. Res.* **106**: 7263–7279.

Szeto KK, Stewart RE. 1997. Effects of melting on frontogenesis. *J. Atmos. Sci.* **54**: 689–702.

Wernli H. 1997. A Lagrangian-based analysis of extratropical cyclones. II: A detailed case-study. *Q. J. R. Meteorol. Soc.* **123**: 1677–1706.

Wernli H, Davies HC. 1997. A Lagrangian-based analysis of extratropical cyclones. I: The method and some applications. *Q. J. R. Meteorol. Soc.* **123**: 467–489.